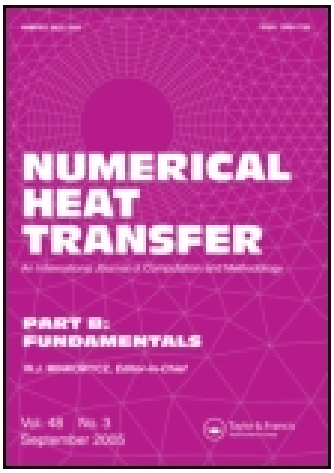

Numerical Heat Transfer, Part B: Fundamentals: An International Journal of Computation and Methodology
Publication details, including instructions for authors and subscription information:
http://www.tandfonline.com/loi/unhb20

Development of a Phase-Field Model for Simulating Dendritic Growth in a Convection-Dominated Flow Field

C. C. Chen [a] & Tony W. H. Sheu [a b]
[a] Center of Advanced Study in Theoretical Sciences , National Taiwan University , Taipei , Taiwan , Republic of China
[b] Department of Engineering Science and Ocean Engineering , National Taiwan University , Taipei , Taiwan , Republic of China
Published online: 23 Oct 2014.

To cite this article: C. C. Chen & Tony W. H. Sheu (2014) Development of a Phase-Field Model for Simulating Dendritic Growth in a Convection-Dominated Flow Field, Numerical Heat Transfer, Part B: Fundamentals: An International Journal of Computation and Methodology, 66:6, 563-585, DOI: 10.1080/10407790.2014.937293

To link to this article: http://dx.doi.org/10.1080/10407790.2014.937293

Numerical Heat Transfer, Part B, 66: 563–585, 2014

ISSN: 1040-7790 print/1521-0626 online
DOI: 10.1080/10407790.2014.937293

Taylor & Francis
Taylor & Francis Group

DEVELOPMENT OF A PHASE-FIELD MODEL FOR SIMULATING DENDRITIC GROWTH IN A CONVECTION-DOMINATED FLOW FIELD

C. C. Chen[1] and Tony W. H. Sheu[1,2]

[1]*Center of Advanced Study in Theoretical Sciences, National Taiwan University, Taipei, Taiwan, Republic of China*

[2]*Department of Engineering Science and Ocean Engineering, National Taiwan University, Taipei, Taiwan, Republic of China*

The effect of flow convection is taken into account in the currently developed phase-field model (PFM) for simulating dendritic growth. In previous PFM studies, flow over a stationary object is wrongly predicted since the predicted velocity magnitude near the fluid–solid interface is not negligibly small. To tackle this problem, the Navier-Stokes equations are solved only in the liquid, while zero flow velocity is prescribed in the stationary object. Simulated results are compared with those computed from two previously proposed models to justify the newly proposed phase-field model.

1. INTRODUCTION

The phase-field model (PFM) has achieved great success over the past few decades in modeling solidification and crystal growth processes [1] for cases involving microstructure [2–5]. The phase-field model adopts a continuous variable to track the interface through addition of a rapid transition function to the flow transport equations. This class of diffuse interface approaches no longer warrants calculation of the Stefan problem subject to a sharp interface of a few nanometers in width unless the interface diffusion length becomes as small as a capillary length. The thin interface model proposed by Karma and Rappel [6, 7] has no necessity for using a diffusive interface with a thickness of a suborder of the tip radius to get the nonuniform temperature along the interface. An interface with a thickness several orders larger than the real thickness in nature can also be used. Adaptive mesh refinement exploiting an extremely wide range of grid spacings can also be adopted to reduce computational demand [8, 9]. The erroneously predicted solute concentration across the thin diffuse interface can be corrected by the antitrapping

Received 10 October 2013; accepted 28 April 2014.

Address correspondence to Tony W. H. Sheu, Department of Engineering Science and Ocean Engineering, National Taiwan University, No. 1, Sec. 4, Roosvelt Road, Taipei, Taiwan 10617, Republic of China. E-mail: twhsheu@ntu.edu.tw

Color versions of one or more of the figures in the article can be found online at www.tandfonline.com/unhb.

NOMENCLATURE

a	coefficient in conservation equation
a_s	anisotropy function
a_1, a_2	constants
A_{nb}	off-diagonal elements of matrix $\underline{\underline{A}}$ in $\underline{\underline{A}}\,\underline{X}=\underline{B}$
A_p	diagonal elements of matrix $\underline{\underline{A}}$ in $\underline{\underline{A}}\,\underline{X}=\underline{B}$
b	coefficient in conservation equation
$\underline{B}$	right-hand side of $\underline{\underline{A}}\,\underline{X}=\underline{B}$
C_D	drag coefficient
C_p	heat capacity
d_0	capillary length
D	dimensionless thermal diffusivity
E	internal energy
f	control face
f_V	enhanced viscosity factor
G	coefficient in conservation equation
h	constant, 2.757
H_L	enthalpy of liquid
H_S	enthalpy of solid
k	heat conductivity
L	domain length
L_W	length of the attached vortex
n_x	x component of unit outward normal vector
n_y	y component of unit outward normal vector
P	pressure
P_{int}	additionally derived pressure
Pr	Prandtl number
R	curvature radius; initial seed radius
Re	Reynolds number
Re_W	Reynolds number defined by interface thickness
t	time
T	temperature
V_{in}	inlet velocity
V_L	velocity in liquid region
V_n	velocity magnitude along the unit outward normal vector (n_x, n_y)
V_x	x component of velocity vector
V_y	y component of velocity vector
W	interface thickness
W_0	length scale
x, y	coordinates
x_n	normal distance from the interface measured from liquid to solid
α	dimensional thermal diffusivity
Γ	coefficient of conservation equation
ΔH	enthalpy of fusion
ΔV	area of control volume
ΔX	grid spacing
ε	anisotropy strength
θ	angle between the normal vector of the interface and the axis of the crystal
λ	coupling constant
μ	viscosity
ρ	density
τ	characteristic time
τ_0	time scale
ϕ	phase variable
ϕ_L	fraction of liquid
ϕ_S	fraction of solid
ϕ	conservation variable

Subscripts

$()_f$	control face
$()_{\mathrm{int}}$	interface
$()_{\max}$	maximum value of the whole domain
$()_{\mathrm{nb}}$	neighboring cell
$()_p$	reference cell
$()_{uu}$	upwind cell for third-order accuracy

Superscripts

$()^{\mathrm{old}}$	previous time step
$()'$	difference from the exact solution
$()^*$	without velocity–pressure coupling

current (ATC) method [10]. This model is particularly useful to avoid the effect of a finite-width interface on the concentration. Some quantitative simulations of directional solidification of alloys have been reported in [11, 12]. Choice of a proper interface thickness in phase-field models turns out to mean a trade-off between accuracy and computational speed.

Since the pioneer works of Fix [13] and Langer [2], the phase-field methods developed for solving interfacial problems have been applied mainly to simulate microstructure formation in solidification [5]. Thanks to the advantage of the phase-field method that avoids direct tracking of the sharp solid–liquid interface, recent progress enables us to more effectively simulate two-phase flow dynamics,

liquid-crystal development, phase transition, polarization in ferroelectric nanostructures, fracture dynamics, vesicle dynamics, viscous fingering, etc.

The phase-field model has been refined by taking the flow motion into account in the simulation of dendritic growth [14, 15]. Tonhardt et al. [15–17] dealt with the momentum equations using an enhanced-viscosity approach to render zero velocity in the solid phase. The effect of fluid flow on the upstream and downstream side branchings has been observed. No quantitative comparison has been made between the theoretical and measured solutions. Beckermann et al. [14] addressed the transport of mass and momentum by residual flow in the diffuse interface region by adding a phase-field-variable dependent advection term to the conservation equations. No-slip condition between liquid and solid was implemented by introducing viscous drag to the diffuse interface region. This model has been frequently used for succinonitrile (SCN) with $\mathrm{Pr} = 23.1$, even when the interface thickness is comparatively larger due to the limitation of computational resources, e.g., $R/W < 5$ [14, 18–22]. Given a PFM parameter in dendritic growth, flow motion may be dominated by viscous force, and the resistance force becomes essential in momentum equations. Even this model has been demonstrated to be applicable to many simulations, but fluid flow near the interface has not been discussed in detail. Actually, the predicted flow velocity still remains nonzero in solids even for simple one-dimensional Poiseuille flow, especially near the interface [14]. Inside a solid, nonzero flow near the fluid–solid interface cannot be eliminated completely. While this problem can be resolved by reducing the interface thickness, such a thickness reduction is not practical because of the accompanying increased computational time. With this in mind, it is paramount to develop a more effective means that falls into the phase-field context.

In this article, nonzero flow in the solid will be shown to play an important role when convection dominates diffusion. Under the circumstances, the resistance force is not large enough to prevent flow passing through the solid. We will demonstrate the efficiency of the proposed model when simulating the convection-dominated case ($\mathrm{Pr} << 1$), which is important in silicon crystal formation. To get rid of the incorrect nonzero flow velocity in the solid, the Navier-Stokes equations in the melt are solved directly, and the results are compared with those computed by two previously proposed models for the simulation of one-dimensional Poiseuille flow and two-dimensional flow over a circular cylinder. The effect of flow in solids is also considered in dendritic growth. In the following sections we briefly describe the phase-field model, then introduce the numerical method in Section 3, and, finally, present the numerical results in Sections 4 and 5. Finally, conclusion will be drawn in Section 6.

2. HYDRODYNAMIC AND PHASE-FIELD EQUATIONS

In this section, hydrodynamic and energy equations are coupled with the equation for the phase-field variable that is used to denote the interface shape. The magnitude of the phase-field variable ϕ defined in $-1 \le \phi \le 1$ is equal to -1 for liquid, 1 for solid, and $\phi = 0$ for the interface. In this article, this scalar variable can be either prescribed or calculated by the user, depending on the case under investigation. The equations for the time-evolving momenta and temperature are introduced first in Section 2.1 and then the equation for the phase-field variable in Section 2.2.

2.1. Hydrodynamic Equations

Dendritic growth from melt has been experimentally and numerically studied more intensively in the diffusion-controlled context. This growth process, dealing with the interplay of heat, mass, and momentum transports, leads to steady-state dendritic tip and unsteady side branching development [20]. In the presence of a buoyancy force that is negligibly small in the melt, flow convection may affect pattern selection and microstructure evolution during solidification. During solidification, flow motion in the melt results from the accompanying dendrite movement and shrinkage. The resulting nonlinear convective hydrodynamic effect, which leads very often to new length and time scales, therefore needs to be accounted for so as to probably get a better predicted morphology [14].

Under the normal dendritic growth condition, the nonuniform temperature distribution can induce thermal convection [23]. The density difference between the solid and liquid phases can induce thermal convection as well [23]. In the presence of gravity, natural convection can also affect the dendritic growth substantially, and can in turn considerably alter dendrite tip development and dendritic side branching. Like many phase field-models [14–17, 24], convection in the melt is taken into account to simulate dendritic growth. Provided that the growth rate is solely dependent on the temperature field, the following energy equation is considered [7]:

$$\rho C_p\left(\frac{\partial T}{\partial t}+V_x\frac{\partial T}{\partial x}+V_y\frac{\partial T}{\partial y}\right)=k\nabla^2 T+\frac{\rho\Delta H}{2}\frac{\partial \phi}{\partial t} \tag{1}$$

Note that

$$\frac{\partial E}{\partial t}=\rho C_p\frac{\partial T}{\partial t}-\frac{\rho\Delta H}{2}\frac{\partial \phi}{\partial t}$$

where E is equal to $\rho\, C_pT+\rho\,(\phi_S H_S+\phi_L H_L)$. The notations ρ, C_p, and k denote the density, heat capacity, and thermal conductivity, respectively. The notation $\Delta H=(H_L-H_S)$ is known as the enthalpy of fusion. For convenience, the fractions of solid and liquid are defined by $\phi_S=(1+\phi)/2$ and $\phi_L=(1-\phi)/2$, respectively.

When melt flow is simulated by phase-field models, momentum equations are normally solved together with the energy equation (1) and the continuity equation given below:

$$\frac{\partial V_x}{\partial x}+\frac{\partial V_y}{\partial y}=0 \tag{2}$$

Two different momentum equations presented below have been employed in the entire computational domain to facilitate the calculation of flow velocity vector $V_{\boldsymbol{x}}$.

Model 1 (Tonhardt [15]).

$$\rho\left(\frac{\partial V_x}{\partial t}+V_x\frac{\partial V_x}{\partial x}+V_y\frac{\partial V_x}{\partial y}\right)=-\frac{\partial P}{\partial x}+\mu\nabla\cdot(f_V\nabla V_x) \tag{3}$$

where f_V is varied with the phase-field variable ϕ according to

$$\begin{cases} f_V = 1 & \phi < -0.6 \\ f_V = 1 + 10(\phi + 0.6)^2 & \text{otherwise} \end{cases} \tag{4}$$

Note that f_V is introduced to increase the viscosity in the solid. Such a numerical resistance force in the momentum vector equation is proportional to the viscosity and the velocity gradient. The resulting magnitude of the enhanced viscosity in the solid can be 25 times greater than the liquid viscosity. While this model makes shear stress to have a magnitude much larger than that in liquid, it generates no stress at all when flow is uniform over a solid, since the externally introduced resistance force is proportional to the velocity gradient.

Model 2 (Beckermann [14]). Within the framework of the PFM, no-slip condition at the solid–liquid interface can be indirectly enforced by adding a dissipative interfacial stress term $2h\mu\varphi_S^2 V_x/W^2$ to the momentum equations. In a thin diffuse interface region, the friction term is considered as a distributed momentum sink. Such a sink can gradually force the liquid velocity to zero as ϕ_S approaches 1. The resulting hydrodynamic equation for V_x, for example, along the x direction is as follows [14].

$$\rho\left[\frac{\partial V_x}{\partial t} + \frac{\partial}{\partial x}\left(\frac{V_x V_x}{\phi_L}\right) + \frac{\partial}{\partial y}\left(\frac{V_y V_x}{\phi_L}\right)\right] = -\phi_L \frac{\partial P}{\partial x} + \mu\nabla^2 V_x - \frac{2h\mu\phi_S^2 V_x}{W^2} \tag{5}$$

In the above vector equation, the velocity $V_{\boldsymbol{x}}$ is defined as $V_x = \phi_L V_{x,L}$ and $V_{x,L}$ denotes the velocity in liquid. The value of h is set to be 2.757 in the theoretical study of Poiseuille flow. When ϕ_L approaches zero, all the terms in Eq. (5) approach zero as well. The minimum value of ϕ_L is prescribed as 0.01 in the simulation.

In the above two models, the phase-field variable appears in the momentum equations. Momentum equations are therefore solved in the whole domain. Such a calculation, however, causes a residual flow to appear in the solidm, especially near the interface. In contrast to the above two models, the following new model developed in detail in Section 3 is aimed to numerically ensure satisfaction of the no-flow condition in the liquid domain:

$$\rho\left(\frac{\partial V_x}{\partial t} + V_x\frac{\partial V_x}{\partial x} + V_y\frac{\partial V_x}{\partial y}\right) = -\frac{\partial P}{\partial x} + \mu\nabla^2 V_x - \frac{\partial P_{\text{int}}}{\partial x} \tag{6}$$

The key to success in applying the presently proposed model lies in the derivation of the last term in (6) on the discrete level in the next section.

2.2. Equation for the Phase-Field Variable

The phase-field model belongs to a class of diffuse-interface methods. This method is manifested itself by approximating a sharp interface as a very narrow diffusive region in the solution domain. In the context of the PFM, the interface condition is replaced by a partial differential equation for modeling of the time-evolving

phase-field variable. This phase field has two distinct values, -1 and 1, in each of the phases. In the region around the physical interface, the introduced phase field varies sharply from the negative unit in one phase to the positive unit in the other phase. The thickness of the diffuse interface region is small but can be mostly resolvable. For an overview of the PFM applied to predict the formation of complex interfacial patterns in solidification and a discussion of the merits of this method, one can refer to [5, 6, 25–27].

For one-dimensional Poiseuille flow and two-dimensional flow over a circular cylinder, the phase-field variable is specified by $\phi = \tanh\left(x_n/\sqrt{2}W\right)$ [7], where x_n denotes the normal distance from the interface in the direction from liquid to solid. As for the dendritic growth problem considered in Section 5, the phase-field equation presented later on is employed.

One can refer to the physically more complex phase-field model of Anderson et al. [24] for inclusion of the convection term $\underline{u}\cdot\nabla\phi$ in the equation governing the time-evolving phase-field variable. The convective Cahn-Hillard equation constructed through the minimization of free energy with respect to ϕ to yield its associated chemical energy was also coupled with the Navier-Stokes equations in the context of multiphase flow simulation [28].

In this study, the employed phase-field equation is as follows [7]:

$$\tau\frac{\partial\phi}{\partial t} = \nabla\cdot\left(W^2\nabla\phi\right) + \phi\left(1-\phi^2\right) - \lambda T\left(1-\phi^2\right)^2 + \frac{\partial}{\partial x}\left(|\nabla\phi|^2 W\frac{\partial W}{\partial\phi_x}\right) + \frac{\partial}{\partial y}\left(|\nabla\phi|^2 W\frac{\partial W}{\partial\phi_y}\right) \tag{7}$$

Employment of the above equation means that the flow has no direct effect on the morphology but can affect only the energy field. The first two terms on the right-hand side of Eq. (7) represent the surface tension for maintaining the interface to be thin [14]. The third term, $\lambda T(1-\phi^2)^2$, denotes the thermally driven force. The last two terms account for the anisotropy effect on the surface tension [29]. The characteristic time and interface thickness are chosen as $\tau = \tau_0 a_s^2$ and $W = W_0 a_s$, respectively. The length scale W_0 is defined as $W_0 \equiv d_0 D/a_1 a_2$ [7]. In W_0, d_0 is the capillary length and $a_1 = 0.8839$, $a_2 = 0.6267$. The time scale τ_0 is defined as $\tau_0 \equiv DW_0^2/\alpha$, where α and D are the dimensional and dimensionless thermal diffusivity, respectively. The coupling constant, λ, is D/a_2 in this study. In (7), the anisotropic function is $a_s = 1+\varepsilon\ (\cos 4\theta)$, where $\varepsilon = 0.05$ and θ denotes the angle between the normal vector of the interface and the axis of the crystal, respectively [7].

3. NUMERICAL METHOD

All the conservation equations can be cast to the following general form [9]:

$$a\frac{\partial\varphi}{\partial t} + \frac{\partial bV_x\varphi}{\partial x} + \frac{\partial bV_y\varphi}{\partial y} = \nabla\cdot(\Gamma\nabla\varphi) + G \tag{8}$$

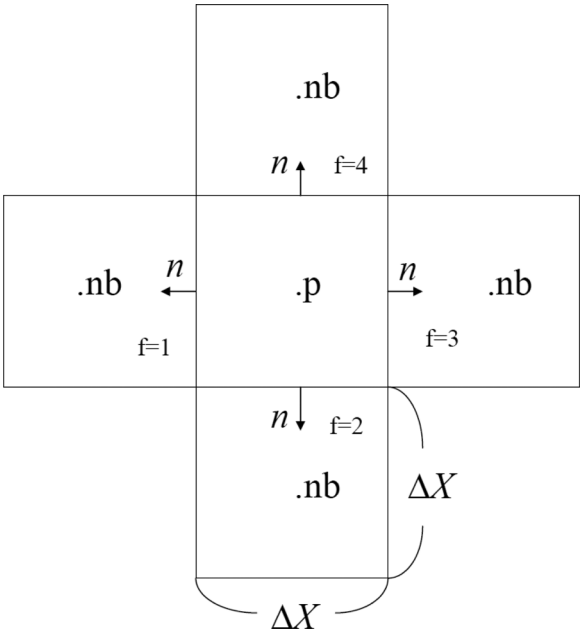

Figure 1. Schematic of the notations used in the present finite-volume method. Note that ΔV is equal to ΔX^2 in the schematic with uniform grid spacing ΔX.

The dependent variable φ stored at the center of the control volume can be either the temperature T, phase-field variable ϕ, pressure P, or velocity components V_x and V_y. The finite-volume method (FVM) is applied to integrate each equation in (8) over a control volume ΔV, shown schematically in Figure 1, to yield the corresponding discrete momentum, energy, and phase-field equations [9]. In this study, the velocity is solved in the liquid phase only for $\phi_p < 0$. The velocity is directly assigned to have zero magnitude in the solid phase for $\phi_p \geq 0$.

By virtue of the divergence theorem, the discretized continuity equation [for $\varphi = 1$, $b = 1$, $a = \Gamma = G = 0$ in (8)] and the x-momentum equation [$\varphi = V_x$, $a = 1$, $b = 1$, $\Gamma = \mu/\rho$, $G = -\frac{\partial P}{\partial x}\frac{\Delta V}{\rho}$ in (8)] can be respectively derived as follows for the velocity $V_{x,p}$ along the x direction at the volume center p:

$$\sum_{f=1}^{4} V_{n,f}\,\Delta X = 0 \tag{9}$$

$$\begin{aligned} &\frac{V_{x,p} - V_{x,p}^{\text{old}}}{\Delta t}\,\Delta V + \sum_{f=1}^{4} V_{n,f} V_{x,f}\,\Delta X \\ &\quad = \sum_{f=1}^{4} \frac{\mu}{\rho}\left(n_x \frac{\partial V_x}{\partial x} + n_y \frac{\partial V_x}{\partial y}\right)\Delta X - \frac{\partial P}{\partial x}\frac{\Delta V}{\rho} \end{aligned} \tag{10}$$

In a cell that does not involve the interface, Eq. (10) can be approximated as follows:

$$\frac{V_{x,p}-V_{x,p}^{\text{old}}}{\Delta t}\Delta V+\sum_{f=1}^{4}V_{n,f}V_{x,f}\Delta X=\sum_{f=1,3}\frac{\mu}{\rho}\frac{(V_{x,\text{nb}}-V_{x,p})}{(x_{\text{nb}}-x_p)}\Delta X+\sum_{f=2,4}\frac{\mu}{\rho}\frac{(V_{x,\text{nb}}-V_{x,p})}{(y_{\text{nb}}-y_p)}\Delta X-\frac{\partial P}{\partial x}\frac{\Delta V}{\rho} \tag{11}$$

The subscript "nb" denotes the neighboring cell centers with respect to the reference cell center p.

In the presence of an interface in a control volume, the right-hand side (RHS) of Eq. (10), derived in detail in Appendix A, is as follows:

$$\begin{aligned}\sum_{f=1}^{4}\frac{\mu}{\rho}\left(n_x\frac{\partial V_x}{\partial x}+n_y\frac{\partial V_x}{\partial y}\right)\Delta X-\frac{\partial P}{\partial x}\frac{\Delta V}{\rho}&=\sum_{f=1,3}\frac{\mu}{\rho}\frac{(V_{x,\text{nb}}-V_{x,p})}{(x_{\text{nb}}-x_p)}\Delta X+\sum_{f=2,4}\frac{\mu}{\rho}\frac{(V_{x,\text{nb}}-V_{x,p})}{(y_{\text{nb}}-y_p)}\Delta X\\&+\sum_{\phi_p\phi_{\text{nb}}\le 0,\,f=1,3}\frac{\mu}{\rho}\left[-\frac{(V_{x,\text{nb}}-V_{x,p})}{(x_{\text{nb}}-x_p)}-\frac{V_{x,p}}{(x_{\text{int}}-x_p)}\right]\Delta X\\&+\sum_{\phi_p\phi_{\text{nb}}\le 0,\,f=2,4}\frac{\mu}{\rho}\left[-\frac{(V_{x,\text{nb}}-V_{x,p})}{(y_{\text{nb}}-y_p)}-\frac{V_{x,p}}{(y_{\text{int}}-y_p)}\right]\Delta X\\&-\frac{\partial P}{\partial x}\frac{\Delta V}{\rho}\end{aligned} \tag{12}$$

Defining the sum of the second and third terms shown in the RHS of (12) as $-\frac{\partial P_{\text{int}}}{\partial x}\frac{\Delta V}{\rho}$, the x-momentum equation in a control volume containing an interface can be rewritten as

$$\begin{aligned}\frac{V_{x,p}-V_{x,p}^{\text{old}}}{\Delta t}\Delta V+\sum_{f=1}^{4}V_{n,f}V_{x,f}\Delta X&=\sum_{f=1}^{4}\frac{\mu}{\rho}\left(n_x\frac{\partial V_x}{\partial x}+n_y\frac{\partial V_x}{\partial y}\right)\Delta X-\frac{\partial(P+P_{\text{int}})}{\partial x}\frac{\Delta V}{\rho}\end{aligned} \tag{13}$$

where $\Delta V=\Delta X^2$ and

$$\begin{aligned}-\frac{\partial P_{\text{int}}}{\partial x}\frac{\Delta V}{\rho}&=\sum_{\phi_p\phi_{\text{nb}}\le 0,f=1,3}\frac{\mu}{\rho}\left[-\frac{(V_{x,\text{nb}}-V_{x,p})}{(x_{\text{nb}}-x_p)}-\frac{V_{x,p}}{(x_{\text{int}}-x_p)}\right]\Delta X\\&+\sum_{\phi_p\phi_{\text{nb}}\le 0,f=2,4}\frac{\mu}{\rho}\left[-\frac{(V_{x,\text{nb}}-V_{x,p})}{(y_{\text{nb}}-y_p)}-\frac{V_{x,p}}{(y_{\text{int}}-y_p)}\right]\Delta X\end{aligned} \tag{14}$$

The superscript "old" denotes the previous time step. Also, V_n represents the velocity component along the unit outward normal n shown schematically in Figure 1. Calculation of $V_{n,f}$ and $V_{x,f}$ is detailed in Appendix B. The interfacial velocity magnitude is assigned to be zero provided that $\phi_p \phi_{\mathrm{nb}} \leq 0$.

The interface location $(x_{\mathrm{int}}, y_{\mathrm{int}})$ is linearly interpolated from the face values ϕ_p and ϕ_{nb} so as to get the zero interface phase-field value, thereby yielding

Table 1. The proposed PFM solution algorithm

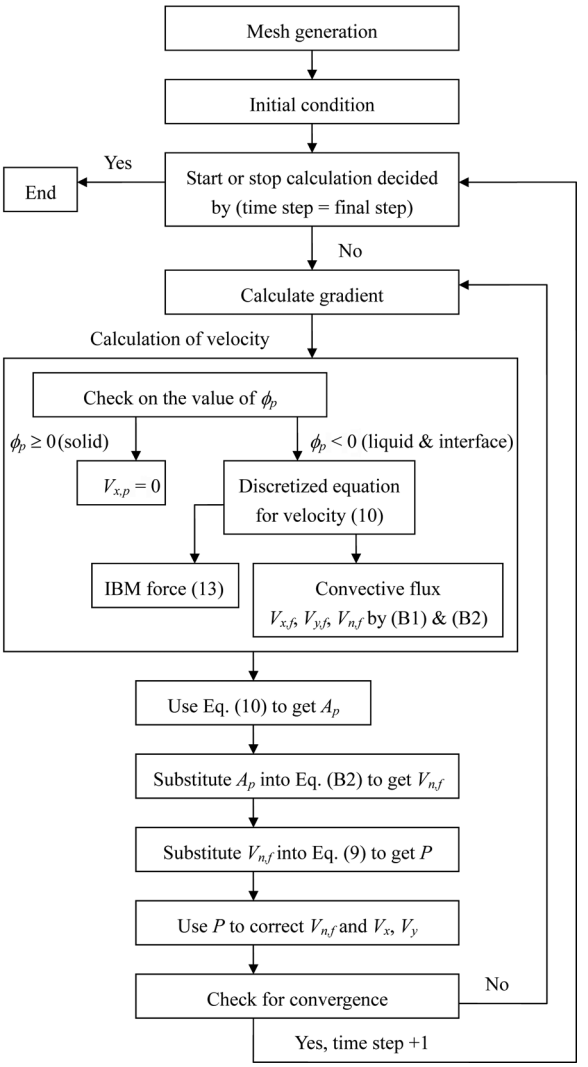

Table 2. Coefficients in the discretized equation $\underline{\underline{A}}\ \underline{X} = \underline{B}$

Solid	Liquid	Interface
$\phi_p \geq 0$	$\phi_p < 0$ & $\phi_{nb} < 0$	$\phi_p < 0$ & $\phi_{nb} \geq 0$
$A_{nb} = 0$	$A'_{nb} = -\frac{\mu}{\rho}\frac{\Delta X}{\lvert x_{nb}-x_p\rvert + \lvert y_{nb}-y_p\rvert}$	$A'_{nb} = -\frac{\mu}{\rho}\frac{\Delta X}{\lvert x_{int}-x_p\rvert + \lvert y_{int}-y_p\rvert}$
	$A_{nb} = w_{nb} V_{n,f}\,\Delta X - \frac{\mu}{\rho}\frac{\Delta X}{\lvert x_{nb}-x_p\rvert + \lvert y_{nb}-y_p\rvert}$	$A_{nb} = w_{nb} V_{n,\,f}\,\Delta X$
$A_p = 1$	$A_p = \frac{\Delta V}{\Delta t} + \sum w_p V_{n,\,f}\,\Delta X - \sum A'_{nb}$	
$B = 0$	$B = -\nabla P\,\Delta V + \frac{V_{x,p}^{old}\Delta V}{\Delta t} - \sum w_{uu} V_{n,f} V_{x,uu}\,\Delta X$	

$$x_{int} = x_p - \left(x_{nb} - x_p\right)\frac{\phi_p}{\left(\phi_{nb} - \phi_p\right)} \tag{15}$$

$$y_{int} = y_p - \left(y_{nb} - y_p\right)\frac{\phi_p}{\left(\phi_{nb} - \phi_p\right)} \tag{16}$$

Note that $-\frac{\partial P_{int}}{\partial x}$ in Eq. (13) is approximately equal to

$$\left\{ \sum_{\phi_p\phi_{nb}\leq 0,\, f=1,3} \left[-\frac{\left(V_{x,nb} - V_{x,p}\right)}{\left(x_{nb} - x_p\right)} - \frac{V_{x,p}}{\left(x_{int} - x_p\right)} \right] + \sum_{\phi_p\phi_{nb}\leq 0,\, f=2,4} \left[-\frac{\left(V_{x,nb} - V_{x,p}\right)}{\left(y_{nb} - y_p\right)} - \frac{V_{x,p}}{\left(y_{int} - y_p\right)} \right] \right\} \frac{\mu\,\Delta X}{\Delta V}$$

detailed in Appendix A. The solution algorithm of the proposed PFM is summarized in Table 1.

Having discretized the momentum equations, we are led to get the matrix equation $\underline{\underline{A}}\ \underline{X} = \underline{B}$ summarized in Table 2, where $\underline{X}$ denotes the velocity vector. The matrix $\underline{\underline{A}}$ is composed of the diagonal element A_p and the off-diagonal element A_{nb}. The term A_p in Eq. (B2) of Appendix B is used to solve the pressure field.

4. NUMERICAL RESULTS

4.1. Poiseuille Flow

The models presented in Section 2 are applied to solve first the one-dimensional Poiseuille flow problem, which is amenable to exact solution. The equations in liquid and solid are as follows for $dP/dy = -2\mu/L^2$:

$$\frac{d^2 V_x}{dx^2} - \frac{1}{\mu}\frac{dP}{dy} = 0 \quad \text{in liquid} \tag{17}$$

$$V_x = 0 \qquad \text{in solid} \tag{18}$$

The computational domain is set from $x = 0$ to $x = 2L$ for the liquid region and from $x = 2L$ to $x = 3L$ for the solid region. No-slip condition is prescribed at the

boundaries, $x=0$ and $x=3L$, and the interface is located at $x=2L$. The resulting exact solution of Eq. (17) is as follows:

$$\frac{V_x}{V_{x,\max}} = 2\frac{x}{L}\left(1-\frac{x}{2L}\right) \quad \text{in liquid,} \tag{19}$$

where $V_{x,\max}=1$.

While applying the phase-field model to solve the Poiseuille problem, the phase-field profile is assumed as follows:

$$\phi = \tanh\left(\frac{x-2L}{\sqrt{2}W}\right) \tag{20}$$

where $W=1$ and $L=5$. The interface thickness chosen in this study is not small in comparison to others. When solving the Poiseuille flow, the simplified governing equations described by Eqs. (3), (5), and (6) can be therefore written as

$$\frac{d}{dx}\left(f_V\frac{dV_x}{dx}\right)+\frac{2}{L^2}=0 \tag{21}$$

$$\frac{d^2V_x}{dx^2}+\phi_L\frac{2}{L^2}-\frac{2h\phi_S^2V_x}{W^2}=0 \tag{22}$$

$$\frac{d^2V_x}{dx^2}+\frac{2}{L^2}-\frac{1}{\mu}\frac{\partial P_{\text{int}}}{\partial y}=0 \quad \text{in liquid and interface} \tag{23}$$

As can be seen from Figure 2, use of the first two models cannot prevent fluid flow in the solid, in particular, when using the Tonhardt model. The resistance force

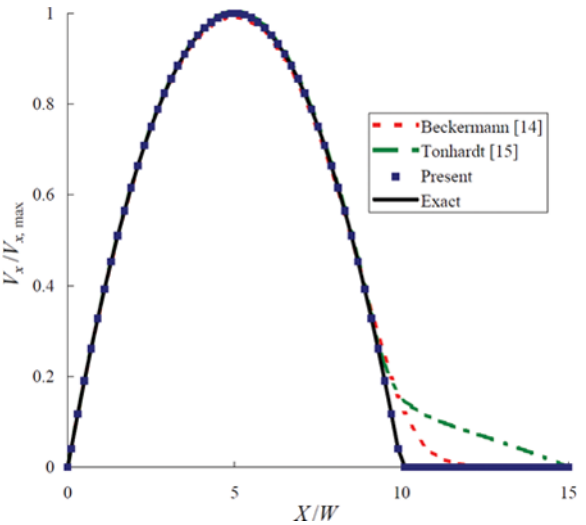

Figure 2. Comparison of the values of $V_x/V_{x,\max}$, predicted at $\Delta X=0.05$, $W=1$, and $L=5$, with respect to the dimensionless length X/W.

is determined by the velocity gradient rather than by the velocity. This may make uniform flow appear in the solid because of the lack of velocity gradient to generate the required resistance force. The resistance force is zero in uniform flow using this model no matter how the viscosity is increased. Provided that a symmetric boundary condition is prescribed at $x = 3L$, when W approaches zero the solution of Eq. (21) can be derived as

$$\frac{V_x}{V_{x,\max}} = \frac{-x^2}{L^2} + \frac{6x}{L} \quad \text{in liquid} \tag{24}$$

$$\frac{V_x}{V_{x,\max}} = \frac{1}{26.6}\left(\frac{-x^2}{L^2} + \frac{6x}{L} + 25.6 \cdot 8\right) \quad \text{in solid} \tag{25}$$

Using the ratio of $V_x/V_{\max} \sim 8$ at the interface, $x = 2L$, it is difficult to yield a no-slip boundary condition.

In the Beckermann model the resistance force exists at the interface and in the whole solid region. The difference between the predicted and exact solutions appears mostly near the interface. The predicted solution agrees well with the exact solution in regions far away from the interface.

The velocity at the interface is further compared for cases investigated at different values of W ranging from 0.002 to 2.5. Since an interface must be present between cells of different sign, which is $\phi_p \phi_{\text{nb}} \leq 0$, the velocity at the interface is calculated according to the following linear interpolation equation:

$$V_{x,\text{int}} = V_{x,p} - \left(V_{x,\text{nb}} - V_{x,p}\right)\frac{\phi_p}{\phi_{\text{nb}} - \phi_p}. \tag{26}$$

Since the slopes of the velocity vectors in the liquid and solid are not equal to each other, the magnitude of $V_{x,\text{int}}$ computed from Eq. (26) is not always equal to zero even if an exact solution is used. Therefore a proper interface velocity is obtained from

$$V'_{x,\text{int}} = V'_{x,p} - \left(V'_{x,\text{nb}} - V'_{x,p}\right)\frac{\phi_p}{\phi_{\text{nb}} - \phi_p} \tag{27}$$

In the above, V'_x denotes the difference between the exact and simulated solutions. The computed interface velocities using the three investigated models are plotted in Figure 3. It can be seen that the Tonhardt model always yields a substantial error no matter how the interface thickness or the grid spacing is decreased.

Unlike the Tonhardt model, ahead of the region $W > \Delta X$ the interface velocity computed from the Beckermann model decreases when the value of W becomes smaller. The applicability of the model depends on the relative dominance of the last term in Eq. (22). Once $W < \Delta X$, no matter how the value of W is decreased, the accuracy will be limited by ΔX. At a fixed value of ΔX, the best value of V'_{int} is about $\Delta X = W$. This value reaches a convergent value, which is 1, when W approaches 0.

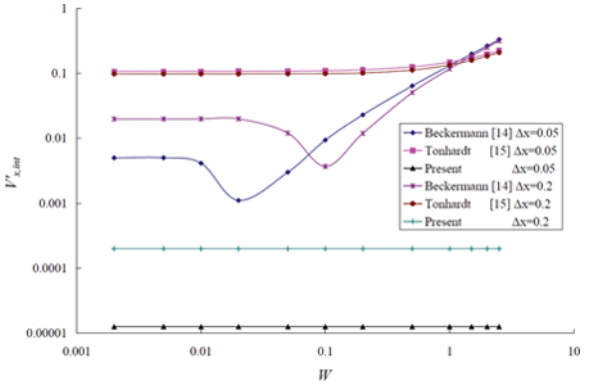

Figure 3. Comparison of the values of $V'_{x,\mathrm{int}}$ shown in (27) with respect to W.

The present model predicts the best result in comparison with those computed from the other two models. The predicted error comes primarily from the discretization, since it is second-order-accurate in most of the uniformly discretized domain.

4.2. Flow over a Two-Dimensional Circular Cylinder

The length of the computational domain in the x direction is $L_x = 30$, and in the y direction $L_y = 1$ and 7.5 are considered. The cylinder is located at $x = 7.5$ and $y = 0$. Only a half-domain is simulated using the prescribed symmetric boundary condition. The Reynolds number, $\mathrm{Re} = 2V_{\mathrm{in}}R\rho/\mu$, is kept at 40 for the chosen values of $V_{\mathrm{in}} = 1$ and $R = 0.5$. The phase field is specified as $\phi = \tanh\left[r - R/\sqrt{2}W\right]$, where the value of W is ranged from 0.0125 to 0.2.

In this section, the first case under consideration is for $L_y = 1$. Comparison of predicted results from two models is made in a smaller y domain to save computation time. For $L_y = 7.5$, the results predicted from the present model are compared with the literature result in [33].

Different values of W and ΔX have been considered for getting the grid-independent result by calculating the length of the attached vortex L_w in the wake. Figure 4 shows the relation between L_w and R/W. Both of the flow fields and the smallest and largest ratios of R/W are also shown. In Eq. (5), the resistance force in the solid is proportional to $1/W^2$, thereby resulting in a small resistance force. Fluid flow passing through the solid is therefore prevented for the case with the smallest value of R/W. The value of W must be small enough to prevent flow passing through the solid, and in Eq. (5) the resistance force prevails. Like the one-dimensional case, the optimum value of L_w is found to appear near $\Delta X = W$, and the proper value of R/W is about 20. Under this circumstance, $\mathrm{Re}_w = V_{\mathrm{in}}W\rho/\mu$ should be equal to or smaller than 1 for the case investigated at $\mathrm{Re} = 40$.

Unlike the Beckermann model, the result obtained from the present model is not sensitive to the magnitude of W because the order of each term in Eq. (6) does not change with W. Only the flux at the interface is slightly different, due to the variation of x_{int} and y_{int} in Eqs. (15) and (16). The advantage of employing the present

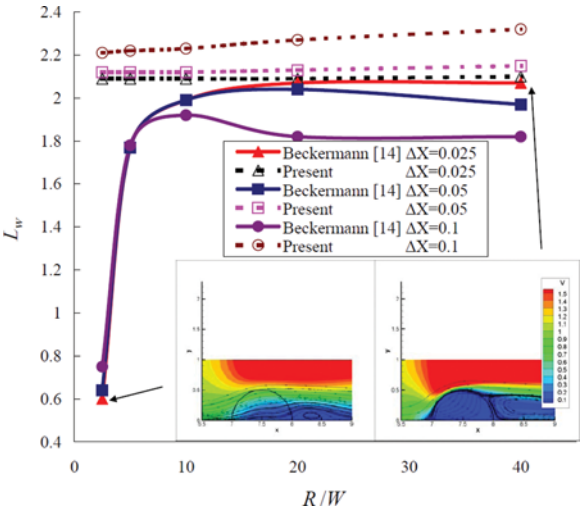

Figure 4. Plot of the values of L_w versus R/W using the Beckermann [14] and the present models. The values of $\phi_L V_L$ predicted by the Beckermann model are plotted for the largest and smallest R/W cases at $\Delta X = 0.025$. The contour levels are ranged from $0.1V_{\text{in}}$ to $1.5V_{\text{in}}$ with the interval $0.1V_{\text{in}}$.

Table 3. Vortex lengths L_w and drag coefficients C_d predicted at different values of ΔX using the present model

	L_w	C_d
Present $\Delta X = 0.1$	2.43	1.678
Present $\Delta X = 0.05$	2.27	1.642
Present $\Delta X = 0.025$	2.25	1.648
Literature [33]	$2.18 \sim 2.55$	$1.48 \sim 1.78$

model without the limitation of W is shown. The result predicted from the present model is also compared with results in the literatures [33] using the same parameters for the case with $L_y = 7.5$. The pressure and velocity gradient are used to calculate the drag coefficient C_d. As shown in Table 3, the predicted values of C_d and L_w have very good agreement with the results in [33].

5. DENDRITIC GROWTH IN CONVECTION FLOW ENVIRONMENT

When the surrounding flow motion is taken into account in dendritic growth simulation, the temperature and phase-field values need to be solved from Eqs. (1) and (7), respectively. The flow field can be calculated from the following dimensionless equations using either the Beckermann model,

$$\frac{\partial V_x}{\partial t} + \frac{\partial}{\partial x}\left(\frac{V_x V_x}{\phi_L}\right) + \frac{\partial}{\partial y}\left(\frac{V_y V_x}{\phi_L}\right) = -\phi_L \frac{\partial P}{\partial x} + \text{Pr}\ D\nabla^2 V_x - 2h\ \text{Pr}\ D\phi_S^2 V_x \tag{28}$$

Table 4. Comparison of the crystal shapes predicted from the Beckermann and present PF models; A, B, C denote the small, mild, and large changes, respectively

	$V_{in}=1$	$V_{in}=2$	$V_{in}=4$	$V_{in}=10$
$Pr=23.1$	A	A	A	A
$Pr=2.31$	A	A	A	B
$Pr=0.231$	A	B	B	—
$Pr=0.1$	B	C	C	—

or the present model in the liquid and at the interface,

$$\frac{\partial V_x}{\partial t}+V_x\frac{\partial V_x}{\partial x}+V_y\frac{\partial V_x}{\partial y}=-\frac{\partial P}{\partial x}+\mathrm{Pr}\ D\nabla^2 V_x-\frac{\partial P_{\mathrm{int}}}{\partial x} \tag{29}$$

In the above, $Pr=\mu/\alpha\rho$. The time and length scales for Eqs. (28) and (29) are chosen to be W_0 and τ_0. The pressure is rescaled by density. From the previous two tests we know that the flow predicted by the Beckermann model can pass through the solid. With this in mind, it is paramount to tackle this problem. A prevalent feature of the proposed PFM is the strong similarity between the derived term in (29) and the momentum-forcing term added to the immerse-boundary method [35].

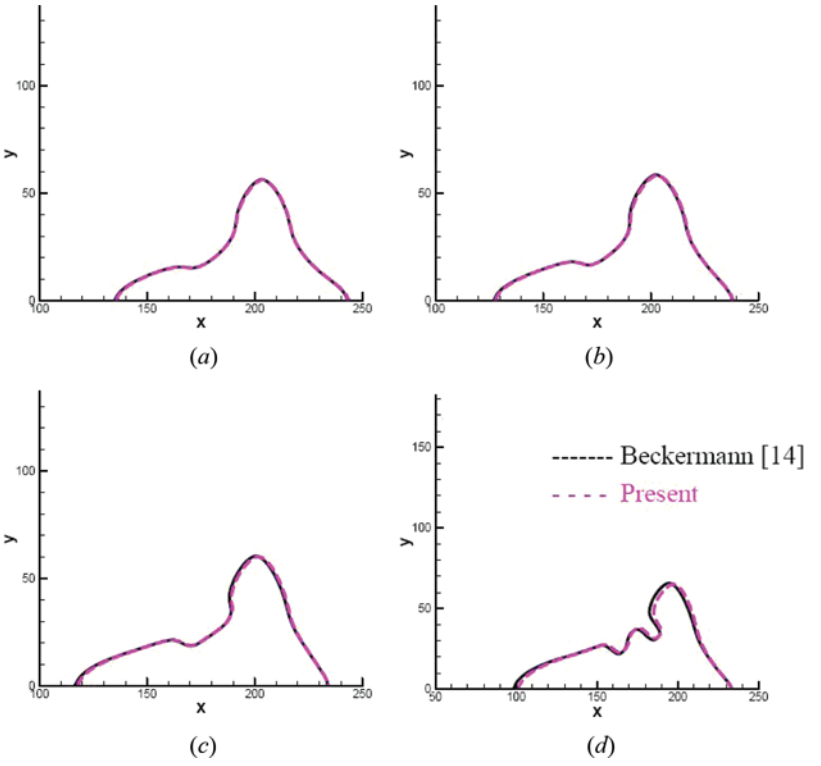

Figure 5. Comparison of the crystal shapes for the case investigated at $Pr=23.1$ under different inlet velocities: (*a*) $V_{in}=1$; (*b*) $V_{in}=2$; (*c*) $V_{in}=4$; (*d*) $V_{in}=10$.

The dimensionless initial temperature T is set at -0.55 in the liquid and at 0 in the initial circular seed with $R = 3$. The dimensionless thermal diffusivity is $D = 4$. Similar to the model considered in [20], the present phase-field model employed to simulate dendritic growth is assumed not to be advected with flow.

Unlike the two previous benchmark tests, the interface thickness is usually chosen to be slightly smaller than the tip radius. Therefore the last two terms in Eq. (28) have the same order of Pr DV_{in}, where V_{in} is the inlet velocity at the left boundary. In other words, the magnitude of resistance force usually has the same order as the viscous force.

For the sake of making comparison between the proposed and Beckermann models applied in diffusion and convection regimes, we perform a series of calculations at different Prandtl numbers Pr and inlet velocities V_{in}. As inlet velocity becomes increasingly larger and/or the Prandtl number becomes smaller, convection tends to dominate diffusion. With these two facts in mind, simulation for Pr ($= 0.1$, 0.231, 2.31, 23.1) and V_{in} ($= 1$, 2, 4, 10) will be carried out to elucidate their effect on the growth of crystals. In these simulations, we are also aiming for a flavor of the degree of difference between the current and the Beckermann models.

The results in Figures 5–8 for the respective values of Pr are plotted with respect to the different values of inlet velocity. One can clearly see from these figures that as convection increasingly dominates diffusion, the growth of crystal loses its stability to

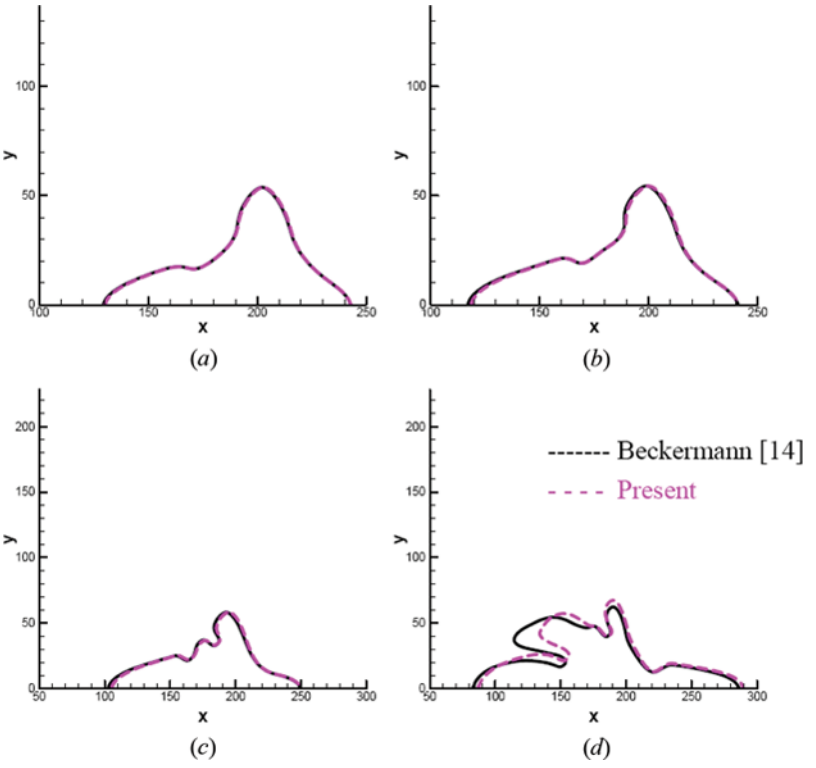

Figure 6. Comparison of the crystal shapes for the case investigated at Pr = 2.31 under different inlet velocities: (*a*) $V_{\text{in}} = 1$; (*b*) $V_{\text{in}} = 2$; (*c*) $V_{\text{in}} = 4$; (*d*) $V_{\text{in}} = 10$.

bend the transverse arm toward the upstream direction. Such a noticeable progress of crystal toward the upstream side is the consequence of cooler inlet flow. For completeness, the morphologies predicted by the two models are divided into negligibly small, mildly different, essentially different, and markedly different groups. One can clearly see from Table 4 the dependence of the crystal growth on the degree of flow convection, making the morphologies at high V_{in} and/or low Pr very different from their diffusion-dominant counterparts (low V_{in} and/or high Pr). For completeness, error reductions for V and P are also plotted in Figure 9 with respect to the iteration number for the case, for example, investigated at $V_{in} = 2$ and $\mathrm{Pr} = 23.1$. Our aim here is to provide evidence that the segregated solution algorithm employed in the newly proposed PFM equation can indeed yield fairly good convergent solution behavior.

Good agreement with the other quantitative simulations [14, 18–22] carried out at higher values of Pr is shown. For the case $\mathrm{Pr} << 1$, such as silicon, the contribution of the resistance term in Eq. (28) can be greatly reduced and flow in the solid may be significantly different from zero. We then consider the case with the value of Pr being decreased to 0.1, such that the resulting flow becomes dominated by the convection force. As shown in the last two figures, the flow can pass through the solid from the upstream side, especially, at the transverse arm having the shortest streamwise

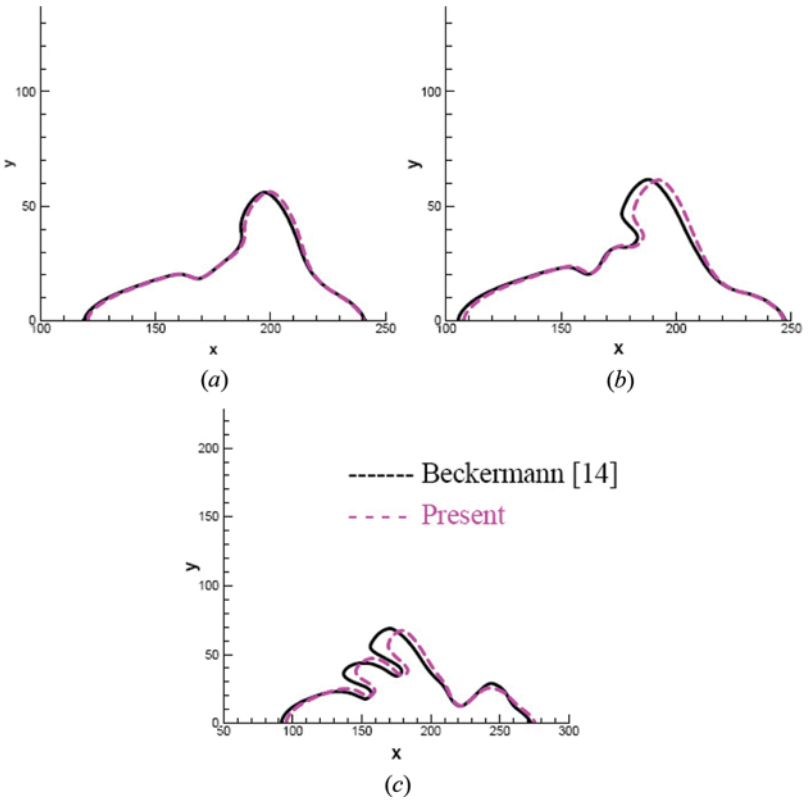

Figure 7. Comparison of the crystal shapes for the case investigated at $\mathrm{Pr} = 0.231$ under different inlet velocities: (*a*) $V_{in} = 1$; (*b*) $V_{in} = 2$; (*c*) $V_{in} = 4$.

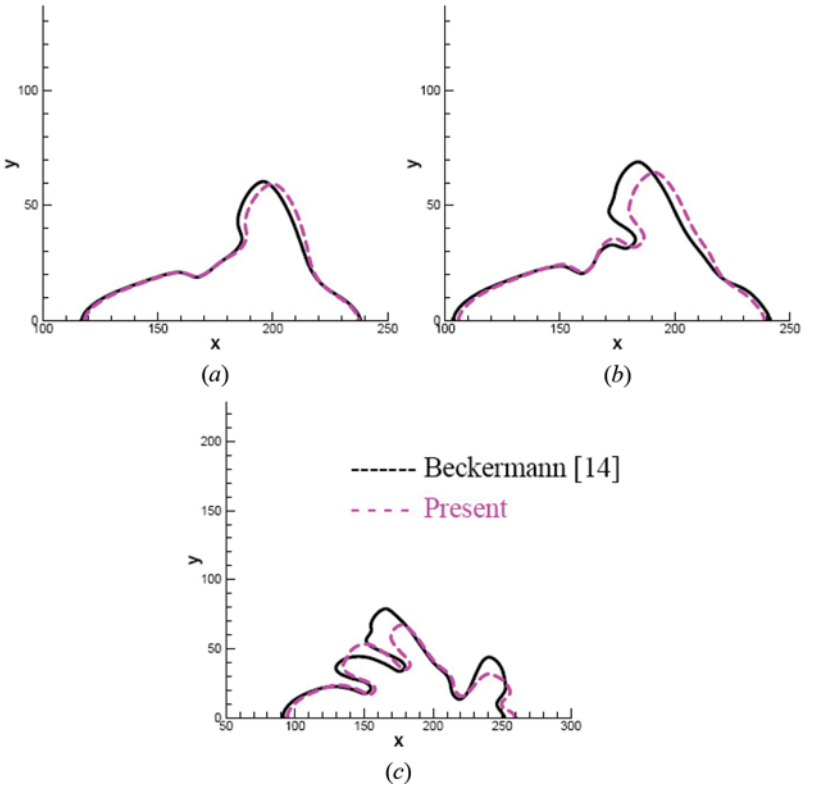

Figure 8. Comparison of the crystal shapes for the case investigated at $\mathrm{Pr} = 0.1$ under different inlet velocities: (*a*) $V_{\mathrm{in}} = 1$; (*b*) $V_{\mathrm{in}} = 2$; (*c*) $V_{\mathrm{in}} = 4$.

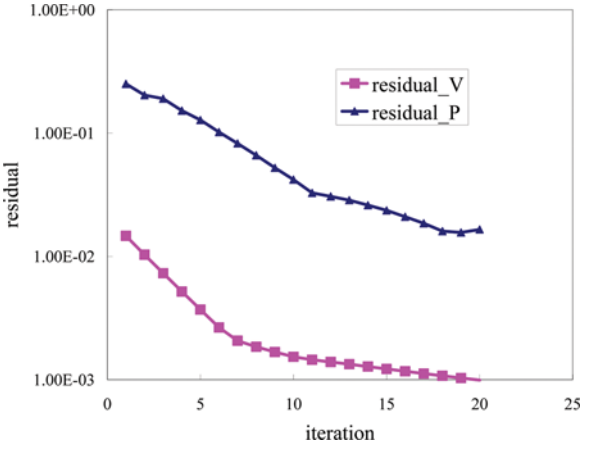

Figure 9. Plot of residual versus iteration for the case investigated at $\mathrm{Pr} = 23.1$ and $V_{\mathrm{in}} = 2$.

crystal width. The flow can bring in unheated melt to the interface and therefore renders undercooling in the process of solidification. Flow in the solid may overpredict the growth rate near the transverse arm using the Beckermann model.

The difference of morphology predicted at a mild overcooling condition is also compared. As shown in Figure 6, the growth rates of the tip at the upstream are significantly different from those at overcooling conditions. The thermal boundary layers at different overcooling conditions are quite different as well [34]. At a condition of considerable overcooling, the thermal boundary layer is thin. Therefore, the heat of solidification released from the upstream side does not easily diffuse to other regions. The tip at the transverse arm has the shortest streamwise crystal width, and overcooling is supplied mainly by the unheated fluid from the surroundings. At a slightly overcooling condition, the thermal boundary layer becomes thicker. The heat of solidification released from the upstream side is transported along the transverse direction. Even when the transverse side has the shortest crystal width, our predicted flow does not pass through the solid. In the Beckermann model, the degree of overcooling is not enough to yield solidification at the transverse arm. Therefore, an accurate model that can actually prevent fluid flow passing though the solid is quite important.

6. CONCLUSIONS

Two different PFM models have been investigated together with the newly proposed model in this study. If the resistance force becomes large enough, the Beckermann model is applicable. High accuracy can be obtained when diffusion dominates convection in the case of dendritic growth. Due to the computational limitation, the interface thickness is usually chosen to have the order of the tip radius, which can greatly reduce resistance. Once convection dominates diffusion, the resistance in the solid cannot prevent fluid flow passing through the solid, and the simulated morphology can be quite different. Application of the present model to prevent flow in the solid is necessary.

FUNDING

The authors would like to acknowledge financial support under National Science Council NSC 101-2811-M-002-165.

REFERENCES

1. M. Asta, C. Beckermann, A. Karman, W. Kurz, R. Napolitano, M. Plapp, G. Purdy, M. Rappaz, and R. Trivedi, Solidification Microstructures, and Solid-State Parallels: Recent Development, Future Directions, *Acta Mater.*, vol. 57, pp. 941–971, 2009.
2. J. S. Langer, Models of Pattern Formation in First-Order Phase Transitions, in G. Grinstein and G. Mazenko (eds.), *Directions in Condensed Matter Physics*, p. 165, World Scientific, New York, 1986.
3. W. Wheeler, G. McFadden, and W. Boettinger, Phase-Field Model for Solidification of a Eutectic Alloy, *Proc. Roy. Soc. Lond., Ser. A*, vol. 452, pp. 495–525, 1996.
4. D. U. Furrer, Application of Phase-Field Modeling to Industrial Materials and Manufacturing Processes, *Curr. Opin. Solid State Mater. Sci.*, vol. 15, pp. 134–140, 2011.

5. W. J. Boettinger, J. A. Warren, C. Beckermann, and A. Karma, Phase-Field Simulation of Solidification, *Annu. Rev. Mater. Res.*, vol. 32, pp. 163–194, 2002.
6. A. Karma and W.-J. Rappel, Phase-Field Method for Computationally Efficient Modeling of Solidification with Arbitrary Interface Kinetics, *Phys. Rev. E*, vol. 53, pp. R3017–R3020, 1996.
7. A. Karma and W.-J. Rappel, Quantitative Phase-Field Modeling of Dendritic Growth in Two and Three Dimensions, *Phys. Rev. E*, vol. 57, pp. 4323–4349, 1998.
8. N. Provatas, N. Goldenfeld, and J. Dantzig, Efficient Computation of Dendritic Microstructures Using Adaptive Mesh Refinement, *Phys. Rev. Lett.*, vol. 80, pp. 3308–3311, 1998.
9. C. W. Lan, C. C. Liu, and C. M. Hsu, An Adaptive Finite Volume Method for Incompressible Heat Flow Problems in Solidification, *J. Comput. Phys.*, vol. 178, pp. 464–497, 2002.
10. A. Karma, Phase-Field Formulation for Quantitative Modeling of Alloy Solidification, *Phys. Rev. Lett.*, vol. 87, pp. 115701-1-4, 2001.
11. B. Echebarria, R. Folch, A. Karma, and M. Plapp, Quantitative Phase-Field Model of Alloy Solidification, *Phys. Rev. E*, vol. 70, pp. 061604-1-22, 2004.
12. Y. L. Tsai, C. C. Chen, and C. W. Lan, Three-Dimensional Adaptive Phase Field Modeling of Directional Solidification of a Binary Alloy: 2D-3D Transition, *Int. J. Heat Mass Transfer*, vol. 53, pp. 2272–2283, 2010.
13. G. J. Fix, Phase Field Methods for Free Boundary Problems, in A. Fasano and M. Primicerio (eds.), *Free Boundary Problems: Theory and Applications*, pp. 580–589, Pitman Advanced Publishing Program, Boston, 1983.
14. C. Beckermann, H.-J. Diepers, I. Steinbach, A. Karma, and X. Tong, Modeling Melt Convection in Phase-Field Simulations of Solidification, *J. Comput. Phys.*, vol. 154, pp. 468–496, 1999.
15. R. Tonhardt and G. Amberg, Phase-Field Simulation of Dendritic Growth in a Shear Flow, *J. Crystal Growth*, vol. 194, pp. 406–425, 1998.
16. R. Tonhardt and G. Amberg, Dendritic Growth of Randomly Oriented Nuclei in a Shear Flow, *J. Crystal Growth*, vol. 213, pp. 161–187, 2000.
17. R. Tonhardt and G. Amberg, Simulation of Natural Convection Effects on Succinonitrile Crystals, *Phys. Rev. E*, vol. 62, pp. 828–836, 2000.
18. Y. Lu, C. Beckermann, and J. C. Ramirez, Three-Dimensional Phase-Field Simulation of the Effect of Convection on Free Dendritic Growth, *J. Crystal Growth*, vol. 280, pp. 320–334, 2005.
19. X. Tong, C. Beckermann, and A. Karma, Velocity, and Shape Selection of Dendritic Crystals in a Forced Flow, *Phys. Rev. E*, vol. 61, pp. R49–R52, 2000.
20. X. Tong, C. Beckermann, A. Karma, and Q. Li, Phase-Field Simulations of Dendritic Crystal Growth in a Forced Flow, *Phys. Rev. E*, vol. 63, pp. 061601-1-15, 2001.
21. J.-H. Jeong, N. Goldenfeld, and J. A. Dantzig, Phase Field Model for Three-Dimensional Dendritic Growth with Fluid Flow, *Phys. Rev. E*, vol. 64, pp. 041602-1-14, 2001.
22. C. C. Chen, Y. L. Tsai, and C. W. Lan, Adaptive Phase Field Simulation of Dendritic Crystal Growth in Forced Flow: 2D vs 3D Morphologies, *Int. J. Heat Mass Transfer*, vol. 52, pp. 1158–1166, 2009.
23. P. Zhao, J. C. Heinrich, and D. R. Poirier, Dendritic Solidification Binary Alloys with Free and Forced Convection, *Int. J. Numer. Meth. Fluids*, vol. 49, pp. 233–266, 2005.
24. D. M. Anderson, G. B. McFadden, and A. A. Wheeler, A Phase-Field Model of Solidification with Convection, *Physica D*, vol. 135, pp. 175–194, 2000.
25. H. S. Udaykumar and W. Shyy, Development of a Grid-Supported Marked Particle Scheme for Interface Tracking, AIAA-93–3384, *11th AIAA Computational Fluid Dynamics Conference*, Orlando, FL, 1993.
26. D. Juric and G. Tryggvason, A Front-Tracking Method for Dendritic Solidification, *J. Comput. Phys.*, vol. 123, pp. 127–148, 1996.

27. J.-H. Jeong, J. A. Dantzig, and N. Goldenfeld, Dendritic Growth with Fluid Flow in Pure Materials, *Metall. Mater. Trans. A*, vol. 34A, pp. 459–466, 2003.
28. V. E. Badalassi, H. D. Ceniceros, and S. Banerjee, Computation of Multiphase System with Phase Field Models, *J. Comput. Phys.*, vol. 190, pp. 371–397, 2003.
29. R. Kobayashi, Modeling and Numerical Simulations of Dendritic Crystal Growth, *Physica D*, vol. 63, pp. 410–423, 1993.
30. B. P. Leonard, A Stable and Accurate Convective Modeling Procedure Based on Quadratic Upstream Interpolation, *Comput. Meth. Appl. Mech. Eng.*, vol. 19, pp. 59–98, 1979.
31. S. V. Patankar, *Numerical Heat Transfer and Fluid Flow*, Hemisphere, Washington, DC, 1980.
32. C. M. Rhie and W. L. Chow, Numerical Study of the Turbulent Flow past an Airfoil with Trailing Edge Separation, *AIAA J.*, vol. 21, pp. 1525–1532, 1983.
33. T. W. H. Sheu, H. F. Ting, and R. K. Lin, An Immersed Boundary Method for the Incompressible Navier-Stokes Equations in Complex Geometry, *Int. J. Numer. Meth. Fluids*, vol. 56, pp. 877–898, 2008.
34. C. C. Chen and C. W. Lan, Efficient Adaptive Three-Dimensional Phase-Field Simulation of Dendritic Crystal Growth from Various Supercoolings Using Rescaling, *J. Crystal Growth*, vol. 311, pp. 702–706, 2009.
35. R. Mittal and G. Iaccarino, Immersed Boundary Methods, *Annu. Rev. Fluid Mech.*, vol. 37, pp. 239–261, 2005.

APPENDIX A

In the finite-volume method, the volume integration is transformed into the surface integral. When $\phi_p\phi_{\mathrm{nb}} > 0$, the interface does not cross the face. The diffuse flux $\frac{\mu}{\rho}\left(n_x\frac{\partial V_x}{\partial x} + n_y\frac{\partial V_x}{\partial y}\right)$ at control faces can be calculated by the values of V_x at the centers of the reference and its neighboring cells. In Cartesian coordinates, the flux along the x direction, for example, is approximated as $\frac{\mu}{\rho}\frac{\left(V_{x,\mathrm{nb}} - V_{x,p}\right)}{\left(x_{\mathrm{nb}} - x_p\right)}$. When $\phi_p\phi_{\mathrm{nb}} \le 0$, the velocity gradients at the interface are different. The diffuse flux at the control face is calculated by the value of V_x at the center of the reference cell and the zero velocity at the interface. The flux is therefore expressed by $-\frac{\mu}{\rho}\frac{V_{x,p}}{\left(x_{\mathrm{int}} - x_p\right)}$. The discrete momentum equation can be written as follows:

$$
\begin{aligned}
&\frac{V_{x,p} - V_{x,p}^{\mathrm{old}}}{\Delta t}\Delta V + \sum_{f=1}^{4} V_{n,f}V_{x,f}\Delta X \\
&= \sum_{f=1}^{4}\frac{\mu}{\rho}\left(n_x\frac{\partial V_x}{\partial x} + n_y\frac{\partial V_x}{\partial y}\right)\Delta X - \frac{\partial P}{\partial x}\frac{\Delta V}{\rho} \\
&= \sum_{\phi_p\phi_{\mathrm{nb}}>0,\, f=1,3}\frac{\mu}{\rho}\frac{\left(V_{x,\mathrm{nb}} - V_{x,p}\right)}{\left(x_{\mathrm{nb}} - x_p\right)}\Delta X + \sum_{\phi_p\phi_{\mathrm{nb}}>0,\, f=2,4}\frac{\mu}{\rho}\frac{\left(V_{x,\mathrm{nb}} - V_{x,p}\right)}{\left(y_{\mathrm{nb}} - y_p\right)}\Delta X \qquad \text{(A1)} \\
&\quad - \sum_{\phi_p\phi_{\mathrm{nb}}\le 0,\, f=1,3}\frac{\mu}{\rho}\frac{V_{x,p}}{\left(x_{\mathrm{int}} - x_p\right)}\Delta X - \sum_{\phi_p\phi_{\mathrm{nb}}\le 0,\, f=2,4}\frac{\mu}{\rho}\frac{V_{x,p}}{\left(y_{\mathrm{int}} - y_p\right)}\Delta X \\
&\quad - \frac{\partial P}{\partial x}\frac{\Delta V}{\rho}
\end{aligned}
$$

The term $-\frac{V_{x,p}}{(x_{\text{int}}-x_p)}$ can be written as $\frac{(V_{x,\text{nb}}-V_{x,p})}{(x_{\text{nb}}-x_p)}-\frac{(V_{x,\text{nb}}-V_{x,p})}{(x_{\text{nb}}-x_p)}-\frac{V_{x,p}}{(x_{\text{int}}-x_p)}$. The right-hand side of (A1) is further written as

$$\begin{aligned}\text{RHS} = &\sum_{f=1,3}\frac{\mu}{\rho}\frac{(V_{x,\text{nb}}-V_{x,p})}{(x_{\text{nb}}-x_p)}\Delta X+\sum_{f=2,4}\frac{\mu}{\rho}\frac{(V_{x,\text{nb}}-V_{x,p})}{(y_{\text{nb}}-y_p)}\Delta X\\ &+\sum_{\phi_p\phi_{\text{nb}}\le 0,f=1,3}\frac{\mu}{\rho}\left[-\frac{(V_{x,\text{nb}}-V_{x,p})}{(x_{\text{nb}}-x_p)}-\frac{V_{x,p}}{(x_{\text{int}}-x_p)}\right]\Delta X\\ &+\sum_{\phi_p\phi_{\text{nb}}\le 0,f=2,4}\frac{\mu}{\rho}\left[-\frac{(V_{x,\text{nb}}-V_{x,p})}{(y_{\text{nb}}-y_p)}-\frac{V_{x,p}}{(y_{\text{int}}-y_p)}\right]\Delta X\\ &-\frac{\partial P}{\partial x}\frac{\Delta V}{\rho}\end{aligned} \tag{A2}$$

Provided $\phi_p\phi_{\text{nb}}\le 0$, the additional force added to the momentum equations helps to yield the physically correct velocity at the fluid–solid interface. By defining

$$\begin{aligned}-\frac{\partial P_{\text{int}}}{\partial x}\frac{\Delta V}{\rho} = &\sum_{\phi_p\phi_{\text{nb}}\le 0,\,f=1,3}\frac{\mu}{\rho}\left[-\frac{(V_{x,\text{nb}}-V_{x,p})}{(x_{\text{nb}}-x_p)}-\frac{V_{x,p}}{(x_{\text{int}}-x_p)}\right]\Delta X\\ &\sum_{\phi_p\phi_{\text{nb}}\le 0,\,f=2,4}\frac{\mu}{\rho}\left[-\frac{(V_{x,\text{nb}}-V_{x,p})}{(y_{\text{nb}}-y_p)}-\frac{V_{x,p}}{(y_{\text{int}}-y_p)}\right]\Delta X\end{aligned} \tag{A3}$$

the x equation, for example, employed in a cell containing an interface becomes

$$\begin{aligned}&\frac{V_{x,p}-V_{x,p}^{\text{old}}}{\Delta t}\Delta V+\sum_{f=1}^{4}V_{n,f}V_{x,f}\Delta X\\ &=\sum_{f=1,3}\frac{\mu}{\rho}\frac{(V_{x,\text{nb}}-V_{x,p})}{(x_{\text{nb}}-x_p)}\Delta X+\sum_{f=2,4}\frac{\mu}{\rho}\frac{(V_{x,\text{nb}}-V_{x,p})}{(y_{\text{nb}}-y_p)}\Delta X\\ &\quad-\frac{\partial(P+P_{\text{int}})}{\partial x}\frac{\Delta V}{\rho}\end{aligned} \tag{A4}$$

It is worthwhile to note that the newly derived term $-\frac{\partial P_{\text{int}}}{\partial x}$ in the above equation provides a new way of looking at the phase-field method.

APPENDIX B

In Eq. (10), $V_{n,f}$ and $V_{x,f}$ are evaluated differently to get a third-order-accurate upwinding scheme. The value of $V_{x,f}$ at the control face shown in Figure 1 is calculated using the QUICK scheme [30], and it is written as

$$V_{x,f} = w_p V_{x,p} + w_{\text{nb}} V_{x,\text{nb}} + w_{uu} V_{x,uu} \tag{B1}$$

The subscript *uu* denotes a cell that does not belong to the reference and its neighboring cells. In uniform meshes, the weighting coefficients w_p and w_{nb} can be derived easily as 0.75, 0375, depending on the upwinding direction, and $w_{uu} = -0.125$.

In the currently employed segregated solution algorithm, the velocity and pressure are solved using the SIMPLE algorithm [31]. The face velocities $V_{n,f}$ in the outward normal direction in Eqs. (9) and (10) are evaluated by the method of Rhie-Chow interpolation [32], and their values in the x direction are written as

$$V_{n,f} = V^*_{n,f} - \frac{\Delta V_p + \Delta V_{\mathrm{nb}}}{A_{p,p} + A_{p,\mathrm{nb}}} \left(\frac{P_{\mathrm{nb}} - P_p}{x_{\mathrm{nb}} - x_p} - \nabla P_{n,f} \right) \tag{B2}$$

The outward normal velocity $V^*_{n,f}$ has been linearly weighted by the velocities of the reference and neighboring cells directly, without the coupling of pressure. The subscript n denotes the outward normal direction to the interface, i.e., $V_{n,f}$ denotes V_x and $-V_x$ at the east and west faces, respectively. The subscript f denotes a value that is linearly weighted by the reference and neighboring cells. The resulting values of $V_{n,f}$ with the velocity–pressure coupling in Eq. (B2) are then used to predict the pressure field from the discretized continuity equation.